AGU PUBLICATIONS

JGR

Journal of Geophysical Research: Planets

RESEARCH ARTICLE

10.1002/2017JE005362

**Key Points:**
- The relationship between elevation and crustal density rules out Pratt isostasy as a major compensation mechanism on the Moon
- Lunar gravity and topography data are consistent with isostatic support of highlands topography by an Airy mechanism
- Highlands terrain likely formed early in lunar history, preceding development of a thick elastic lithosphere

**Correspondence to:**
M. M. Sori,
sori@lpl.arizona.edu

**Citation:**
Sori, M. M., James, P. B., Johnson, B. C., Soderblom, J. M., Solomon, S. C., Wieczorek, M. A., & Zuber, M. T. (2018). Isostatic compensation of the lunar highlands. *Journal of Geophysical Research: Planets*, *123*, 646–665. https://doi.org/10.1002/2017JE005362

Received 6 JUN 2017
Accepted 17 JAN 2018
Accepted article online 7 FEB 2018
Published online 28 FEB 2018



# Isostatic Compensation of the Lunar Highlands

**Michael M. Sori[1], Peter B. James[2,3], Brandon C. Johnson[4], Jason M. Soderblom[5], Sean C. Solomon[6,7], Mark A. Wieczorek[8], and Maria T. Zuber[5]**

[1]Lunar and Planetary Laboratory, University of Arizona, Tucson, AZ, USA, [2]Lunar and Planetary Institute, Houston, TX, USA, [3]Department of Geosciences, Baylor University, Waco, TX, USA, [4]Department of Earth, Environmental and Planetary Sciences, Brown University, Providence, RI, USA, [5]Department of Earth, Atmospheric and Planetary Sciences, Massachusetts Institute of Technology, Cambridge, MA, USA, [6]Lamont-Doherty Earth Observatory, Columbia University, Palisades, NY, USA, [7]Department of Terrestrial Magnetism, Carnegie Institution of Washington, Washington, DC, USA, [8]Laboratoire Lagrange, Observatoire de la Côte d'Azur, Nice, France

**Abstract** The lunar highlands are isostatically compensated at large horizontal scales, but the specific compensation mechanism has been difficult to identify. With topographic data from the Lunar Orbiter Laser Altimeter and gravity data from the Gravity Recovery and Interior Laboratory, we investigate support of highland topography. Poor correlation between crustal density and elevation shows that Pratt compensation is not important in the highlands. Using spectrally weighted admittance, we compared observed values of geoid-to-topography ratio (GTR) with those predicted by isostatic models. Observed GTRs are $25.8^{+7.5}_{-5.7}$ m/km for the nearside highlands and $39.3^{+5.7}_{-6.2}$ m/km for the farside highlands. These values are not consistent with flexural compensation of long-wavelength topography or Airy isostasy defined under an assumption of equal mass in crustal columns. Instead, the observed GTR values are consistent with models of Airy compensation in which isostasy is defined under a requirement of equal pressures at equipotential surfaces at depth. The gravity and topography data thus reveal that long-wavelength topography on the Moon is most likely compensated by variations in crustal thickness, implying that highland topography formed early in lunar history before the development of a thick elastic lithosphere.

## 1. Introduction

Planetary topography, particularly at large horizontal scales, is commonly supported by an isostatic process involving compensating excesses and deficiencies in mass at depth. The highlands of the Moon are generally isostatically compensated (O'Keefe, 1978), and regions of higher elevation have generally greater crustal thickness than regions of lower elevation (Wieczorek et al., 2013). This conclusion, initially drawn from early lunar gravity anomaly maps (Muller & Sjogren, 1968), has persisted with subsequent improvements in data (Zuber et al., 1994; Neumann et al., 1996; Wieczorek et al., 2006, 2013; Andrews-Hanna, 2013). Isostasy can take different forms, including the two classic compensation mechanisms, Airy and Pratt isostasy, as well as flexural isostasy that operates regionally rather than locally. Airy isostasy could result from the floatation of blocks of crustal material of similar composition but different thickness that crystallized in a cooling lunar magma ocean or the lateral redistribution of material from large impacts, whereas Pratt isostasy arising from regional variations in crustal density might be a consequence of variations in the timing of accumulation of early crust in a cooling magma ocean, lateral differences in extent of melting, or repeated redifferentiation of some regions by large impacts (Wetherill, 1975). Identification of the nature of isostatic compensation thus holds promise for elucidating the Moon's early crustal evolution.

A negative correlation between elevation and crustal density inferred from Apollo laser altimetry and geochemical remote sensing data of lunar near-equatorial highland regions suggested that a Pratt isostatic mechanism might be an important component of lunar isostasy (Solomon, 1978). Later data from the Clementine mission (Zuber et al., 1994), however, did not confirm a significant negative correlation between density and elevation in the lunar highlands more generally (Wieczorek & Phillips, 1997) and instead showed that the distribution of the Moon's geoid-to-topography ratio (GTR) is consistent with a single-layer Airy model of the crust or a two-layer Airy model in which upper crustal thickness varies and the lower crust has more nearly uniform thickness. Both studies were restricted to the nearside, owing to the limited coverage of the Apollo data and large uncertainties in the measured geoid of the farside. The GTR calculations were redone (Wieczorek et al., 2006) using gravity data from Lunar Prospector (Konopliv et al., 2001), but those

data also had large uncertainties on the farside. That analysis gave an average GTR for the nearside highlands of 26.7 ± 6.9 m/km. Estimates of lunar crustal thickness have been revised downward since those studies, on the basis of reanalyses of Apollo seismic data (Khan & Mosegaard, 2002; Lognonné et al., 2003) and revised crustal densities (Wieczorek et al., 2013).

Measurements acquired by two recent spacecraft missions allow us to investigate with high-quality observations the isostatic state of the Moon's farside for the first time. The Lunar Orbiter Laser Altimeter (LOLA) (Smith et al., 2016) on the Lunar Reconnaissance Orbiter spacecraft has provided the most well sampled and precise topographic map of any planetary body, and the dual-spacecraft Gravity Recovery and Interior Laboratory (GRAIL) mission (Zuber, Smith, Lehman, et al., 2013) has provided, through spacecraft-to-spacecraft tracking, the highest-resolution global gravity field of any planetary body (Zuber, Smith, Watkins, et al., 2013). The gravity models we used from the GRAIL primary and extended missions (Konopliv et al., 2013, 2014; Lemoine et al., 2013, 2014) were expanded to harmonic degree and order 660, yielding a half-wavelength surface resolution of ~8 km. Such a resolution is a large improvement over the gravity fields available to previous GTR analyses (Wieczorek & Phillips, 1997; Wieczorek et al., 2006), which was expanded to degrees 70 and 150, respectively, corresponding to a half-wavelength surface resolution (Lemoine et al., 1997; Konopliv et al., 2001) of ~73 km and ~36 km. GRAIL maps of the lunar gravity field are 4–5 orders of magnitude more accurate than Clementine maps. Of particular importance is the difference in accuracy for the Clementine and Lunar Prospector geoid maps between the nearside and farside: those models had formal errors ranging from ~2 m in the nearside geoid to ~24 m in the farside geoid (Lemoine et al., 1997; Konopliv et al., 2001) and true uncertainties approximately twice those values (Konopliv et al., 2001). GRAIL gravity fields, in contrast, do not suffer from such a nearside-farside difference in accuracy.

Topographic information has also undergone substantial improvement. Our elevation data come from a LOLA-based topographic map (Smith et al., 2016). LOLA has yielded a topographic model expanded to degree and order 2,500 with ~10 cm precision and ~1 m accuracy. The topographic map following Clementine, in contrast, was derived from the Clementine lidar instrument, which collected topographic measurements (Zuber et al., 1994; Smith et al., 1997) expanded to degree and order 72 with ~10 m precision and ~100 m accuracy. Elevation measurements acquired by the Apollo 15 and 16 laser altimeters (Kaula et al., 1974), which sampled only a limited set of near-equatorial orbital tracks, had ~100 m precision and ~400 m accuracy.

For this paper, we combined the GRAIL gravity and LOLA topography data in two different ways. First, we searched for a signature of negative correlation between elevation and crustal density indicative of Pratt isostasy on more local scales than was possible with data sets available for previous studies. Second, we used the method of spectrally weighted degree-dependent admittances to construct isostatic models that fit the observed GTR values of the lunar highlands. We discuss the results from these procedures as they relate to the structure of the lunar crust and mantle as well as the geophysical evolution of the Moon.

## 2. Elevation-Density Correlations

### 2.1. Methods

To assess the global importance of Pratt isostasy on the Moon, we searched for a negative correlation between elevation and density using LOLA-derived elevation, Lunar-Prospector-derived grain density, and GRAIL-derived bulk density. We used crustal grain density derived from empirical correlations between density and composition (Huang & Wieczorek, 2012) combined with elemental abundances of titanium and iron measured by the Lunar Prospector gamma-ray spectrometer (Prettyman et al., 2006). We used bulk density derived from GRAIL gravity (Wieczorek et al., 2013) and topography data from LOLA (Smith et al., 2016).

We assumed that the composition at or near the lunar surface is representative of that of the underlying crustal column. The lunar highlands have a maximum elevation of ~10 km. A pure Pratt mechanism would imply a crustal density of 2,040 kg/m$^3$ at such an elevation and 2,270 kg/m$^3$ at an elevation of 5 km, given a crustal thickness of 40 km and a crustal density of 2,550 kg/m$^3$ at zero elevation (Wieczorek et al., 2013). These values

can be rejected: if the grain density of the highlands crust were 2,900 kg/m$^3$, a bulk density of 2,040 kg/m$^3$ would require ~30% porosity. Such high porosities do not hold throughout the crust (Wieczorek et al., 2013; Besserer et al., 2014; Soderblom et al., 2015). We can thus rule out a pure Pratt mechanism that involves no relief on one or more interfaces at depth.

We also explored the possibility of Pratt isostasy on regional scales. We applied a moving window of a given radius to maps of elevation, grain density, and bulk density. For each window, we sampled points in a grid pattern at an equidistant nodal spacing of 8 km and determined the correlation coefficient $R$ between density and elevation in that window. At each window location, we plotted the sampled values of grain or bulk density versus elevation, and we calculated the squared correlation coefficient $R^2$ and the slope of the line determined from a least squares fit. A negative slope indicates that Pratt isostasy may be an important contributor to isostasy, and a high $R^2$ value indicates a good fit by a linear relation. We avoided interpretation of windowed areas with a substantial fraction (~10% or more) of maria. Mare basalt deposits were emplaced in topographic lows (Head, 1975), have a higher density than the underlying anorthositic crust (Kiefer et al., 2012), and are much thinner than the crust (Head, 1982); therefore, they are not representative of the composition of the underlying crustal column. Mare regions were defined from digitized U.S. Geological Survey maps (Fortezzo & Hare, 2013). We also avoided interpretation of windowed areas with more than 10% of the area within the large farside South Pole-Aitken (SPA) basin (Head et al., 2010). Points not in either the maria or SPA were considered highlands in this study. We tested for the significance of the resulting set of $R^2$ values by performing a $t$ test, for which the null hypothesis is that the slope of the best fit line between density and elevation at each location is equal to zero. The test statistic is the slope of the best fit line divided by the standard error of the slope. We chose a significance level of 0.05 and rejected the null hypothesis only if the $P$ value associated with the test statistic was less than this significance level.

### 2.2. Results

A map of resulting $R^2$ values is shown in Figure 1 for grain density and elevation measured within 500 km radius windows. For most regions, we do not find a negative correlation between density and elevation at the 95% confidence level. Such a negative correlation is seen and significant primarily in windows that contain both highlands and mare regions, or both highlands and portions of the SPA basin, although a few other localized regions of significance at the 95% level exist. For areas with both highlands and maria, the correlation results from the volcanic emplacement of high-density mare material in topographic lows after formation of the highlands crust rather than Pratt isostasy. We also do not favor short-wavelength Pratt isostasy in the SPA basin, because there is no significant negative correlation in windows that are entirely confined to SPA regions. These general results also hold for cases with 300 and 700 km radius sampling windows, and for cases that considered bulk density instead of grain density. Thus, we find no evidence for a Pratt mechanism for isostatic compensation of topographic relief on regional scales (i.e., several hundred kilometers and greater) in the lunar highlands.

These results do not preclude a global Pratt mechanism operating on the harmonic degree-1 scale. To test this possibility, we searched for a negative correlation between grain density and elevation for all points in the lunar highlands, not just those in a local window. We found a significant (on the basis of the $t$ test described above) negative slope of the best fit line at $-3.27$ kg/m$^3$ per km. This value, however, is a factor of ~20 less than the expected value of ~68 kg/m$^3$ per km for a pure Pratt mechanism (calculated with the equation for Pratt isostasy on a sphere; Wieczorek & Phillips, 1997). Thus, any Pratt component must also be at most minor on the global scale.

## 3. Geoid-to-Topography Ratios

### 3.1. Methods

To test if Airy isostasy is an important mechanism of topographic support, we interpreted GTRs on a sphere using spherical harmonic functions (Wieczorek & Phillips, 1997). We calculated GTR values from the LOLA-derived elevation map and the GRAIL-derived geoid map. For both maps, we excluded spherical harmonic degrees 1 and 2, although our results are robust with respect to this filtering. We determined GTRs by employing a multitaper spectral approach with Slepian windows (Wieczorek & Simons, 2007) (Figure 2).

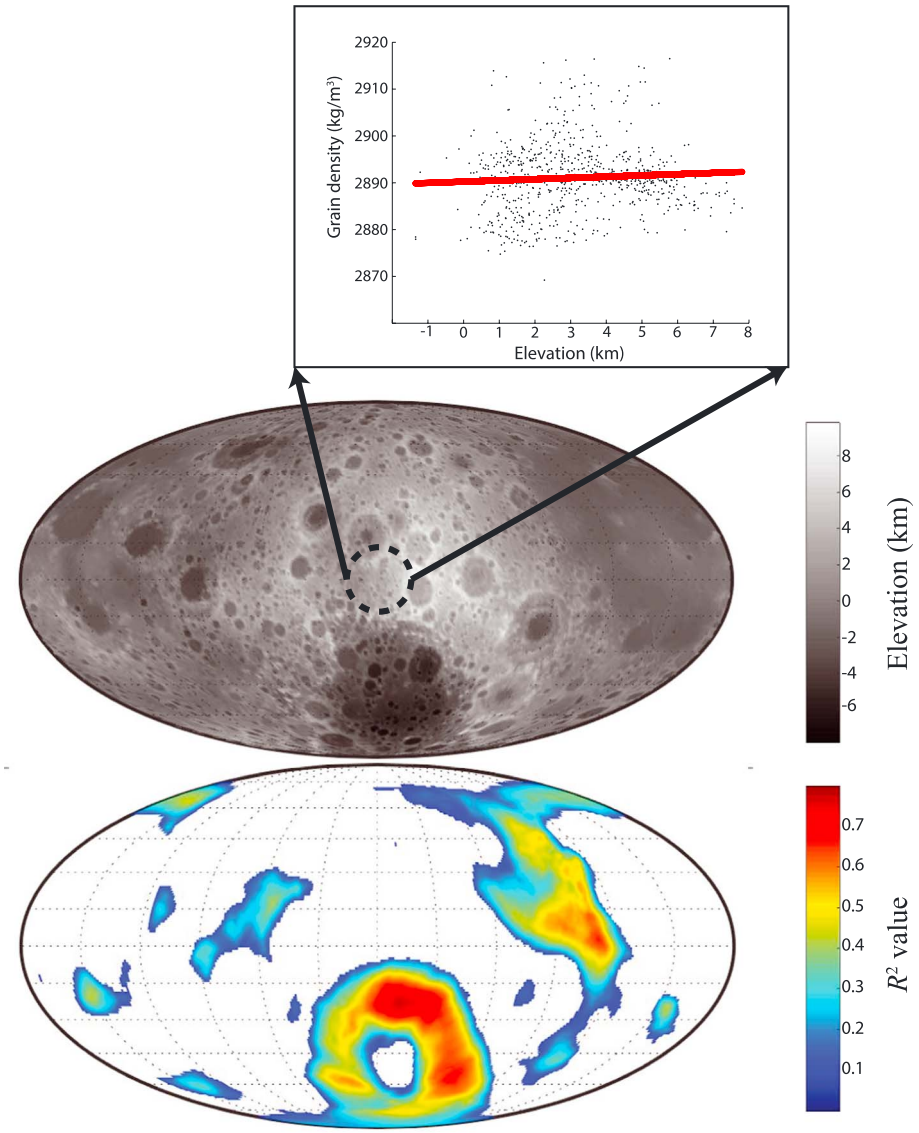


**Figure 1.** Test of a Pratt model for lunar isostasy. $R^2$ values (bottom) for best fit lines of grain density as a function of elevation (middle) within a moving window of 500 km radius. Shown are only $R^2$ values for lines with negative slope values that are statistically significant according to our hypothesis testing. Areas of high $R^2$ value usually occur only when the window includes mare regions or portions of the SPA basin in addition to highland topography. The inset (top) shows one example of the sampled grain density and elevation points (black dots) within a 500 km radius window located at the center of the farside (dashed circle); in this case, we cannot reject the null hypothesis that the slope of the best fit line (red line) is equal to zero. The maps are Mollweide projections centered on the farside.

These observed GTRs were compared with the GTRs predicted by various isostatic models. We considered single-layer Airy models, two-layer Airy models, and a Pratt model. Predicted GTRs were given by a weighted sum of admittances for each spherical harmonic degree (Wieczorek & Phillips, 1997).

The gravitational potential, $U$, exterior to a spherical body can be expressed as

$$U(\mathbf{r}) = \frac{GM}{r}\sum_{l=0}^{\infty}\sum_{m=-l}^{l}\left(\frac{R_0}{r}\right)C_{lm}Y_{im}(\theta,\ \varphi), \tag{1}$$

where $\mathbf{r}$ is position, $G$ is the gravitational constant, $M$ is the mass of the body, $R_0$ is the reference radius of the spherical harmonic coefficients $C_{lm}$ of degree $l$ and order $m$, $Y_{lm}$ is the normalized spherical harmonic function, $\theta$ is the colatitude, and $\varphi$ is the longitude. A given Airy isostatic model on a sphere is equivalent

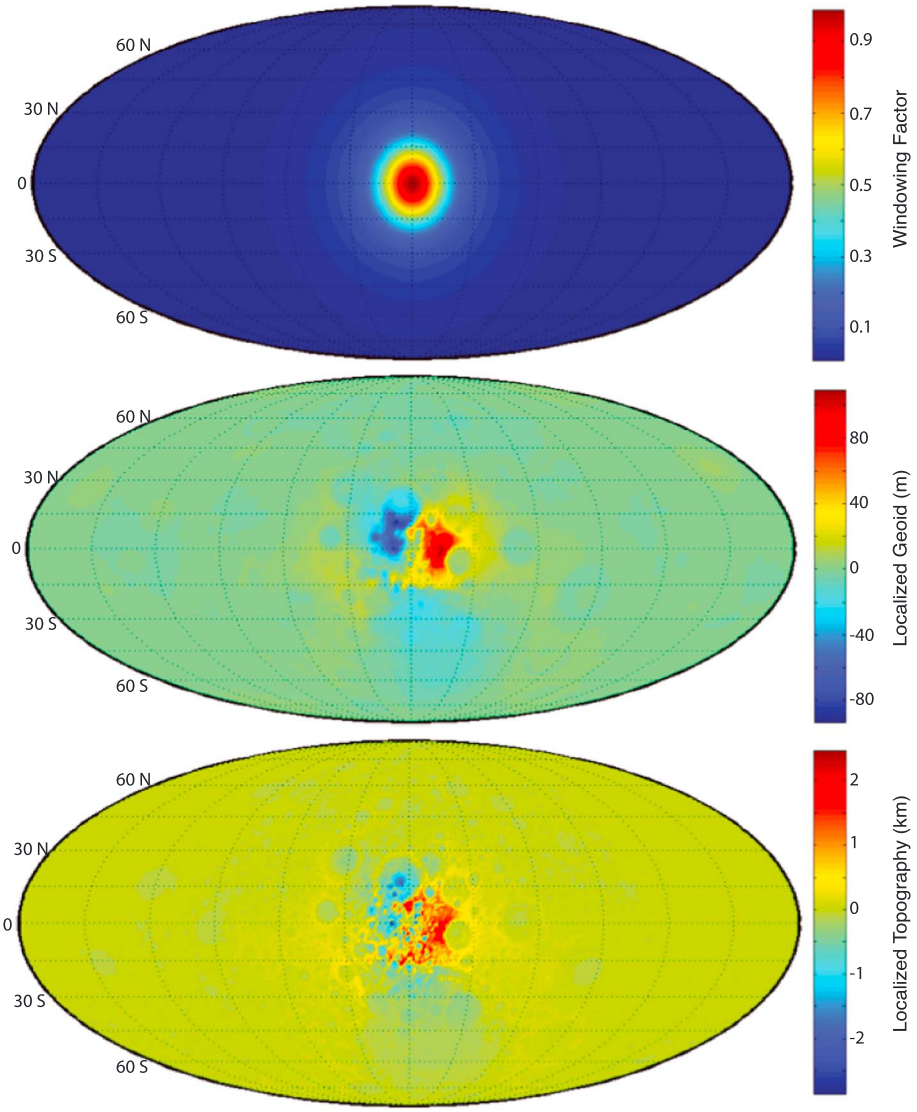


**Figure 2.** Example of localization of our data. This particular Slepian window (top) was constructed to concentrate optimally its power within a spherical cap of radius 750 km while possessing a spherical harmonic bandwidth of 15. The window was applied to the geoid (middle) and topography (bottom). The maps of localized geoid and topography were then converted back to spherical harmonic coefficients, which were used to calculate the GTR from equation (4). The maps are Mollweide projections centered on the farside.

to a sum of spectrally weighted degree-dependent values of the gravity-topography admittance (Wieczorek & Phillips, 1997). The geoid $n$ is defined as the equipotential surface associated with the potential $U$ at a reference radius of 1,738 km. Geoid admittance $Z_l$ is the linear transfer function relating geoid and topography coefficients, given by

$$n_{lm} = Z_l t_{lm}, \tag{2}$$

where $n_{lm}$ and $t_{lm}$ are the spherical harmonic coefficients of the geoid and topography, respectively, at degree $l$ and order $m$.

A previous study (Wieczorek & Phillips, 1997) calculated GTRs on the Moon by fitting a line to geoid and elevation points sampled within a circular window and defining the slope to be the GTR, a procedure followed by others for Venus (Kucinskas et al., 1996) and Mercury (Padovan et al., 2015). Other studies of Venus used cosine tapers to localize topographic fields (Smrekar & Phillips, 1991; James et al., 2013). Here we instead determine GTRs by employing a multitaper approach (Wieczorek & Simons, 2007) with

Slepian windows (Slepian & Pollak, 1961). Slepian windows on a sphere are data tapers that optimize the trade-off between localization and spectral leakage and thus yield a more representative value for a given locality for geophysical problems than other windowing functions. We derived Slepian windows using software (Simons et al., 2006; Harig et al., 2015) for spherical caps of radius 500 km, 750 km, and 1000 km and a tapering bandwidth value of $L = 15$. Use of multiple-sized caps ensures that our results are not sensitive to an arbitrary choice of a single size and allows for a basic analysis of how results change with cap size. All caps were chosen such that their radii are much greater than the half-wavelength resolution of the GRAIL gravity field. For each case, we kept those Slepian windows with corresponding spatial concentration factors >0.99 (i.e., the data tapers for which 99% of the squared area is contained within the spherical cap). For the three cap radii of 500 km, 750 km, and 1000 km, there are one, three, and eight windows, respectively, with spatial concentration factors that meet this constraint. Such windows are the ones we used to localize the geoid and topography (Figure 2). Increasing the tapering bandwidth value $L$ yields more localizing windows with a spatial concentration factor $> 0.99$. For example, $L = 30$ gives 6, 23, and 44 such windows for spherical caps of radius 500 km, 750 km, and 1000 km, respectively.

Degree-1 elevation terms were excluded from the nominal GTR results because there is no gravity signature in center-of-mass coordinates. Degree-2 elevation and geoid terms were excluded because they are likely dominated by tidal and rotational components, including a "fossil bulge," i.e., a component of the lunar shape caused by the tides and rotational flattening early in lunar history (Lambeck & Pullan, 1980; Garrick-Bethell et al., 2010, 2014; Keane & Matsuyama, 2014). Though degree-1 and degree-2 terms were excluded from our nominal results, we discuss the effects of including them below.

We used a moving window approach to estimate the GTR locally. We created localized maps of geoid and topography by moving a Slepian window across the surface of the Moon. We then constructed the spherical harmonic coefficients for localized geoid and topography. The GTR is given by

$$\mathrm{GTR} = \frac{\left(\sum_l S_{TN}(l)\right) - N_{00}T_{00}}{\left(\sum_l S_{TT}(l)\right) - {T_{00}}^2}, \tag{3}$$

where $S_{TN}$ is the cross-power spectrum of functions $T$ and $N$ at degree $l$, $T$ is the localized topography, and $N$ is the localized geoid. If one wishes to assume no offset in the linear fit (i.e., the value of the geoid is zero at zero elevation), the equation simplifies to (Wieczorek, 2015)

$$\mathrm{GTR} = \frac{\sum_l S_{TN}(l)}{\sum_l S_{TT}(l)}. \tag{4}$$

Derivations for equations (3) and (4) are provided in Appendix A. The equations are based on the assumption that topography is referenced to a sphere (Wieczorek & Phillips, 1997). We find that including offsets, as in equation (3), does not change the mode of the distribution of resulting GTRs by more than 3 m/km compared with excluding them, as in equation (4). The localized fields were expanded to spherical harmonic degree and order 660. By repeatedly calculating the GTR in this way, sampling the local geoid and topography in an equidistant grid pattern at a nodal spacing of 30 km, we constructed a global map of GTRs for each Slepian taper, and we then averaged the results across all our chosen tapers at each point to obtain a multitaper estimate of the GTRs for the entire Moon (Figure 3). This averaging process ensures that our results are not sensitive to arbitrarily choosing one specific taper for cases where there are multiple Slepian windows with a spatial concentration factor $> 0.99$. The multitaper method yields several GTR maps for Slepian windows constructed with spherical caps of 750 and 1,000 km radius; we interpreted the standard error of the GTR among those maps at any location as the uncertainty in the GTR.

The predicted GTR for an Airy isostatic model is a weighted sum of admittances, $Z_l$, for each spherical harmonic degree (Wieczorek & Phillips, 1997):

$$\mathrm{GTR} = \sum_l W_l Z_l. \tag{5}$$

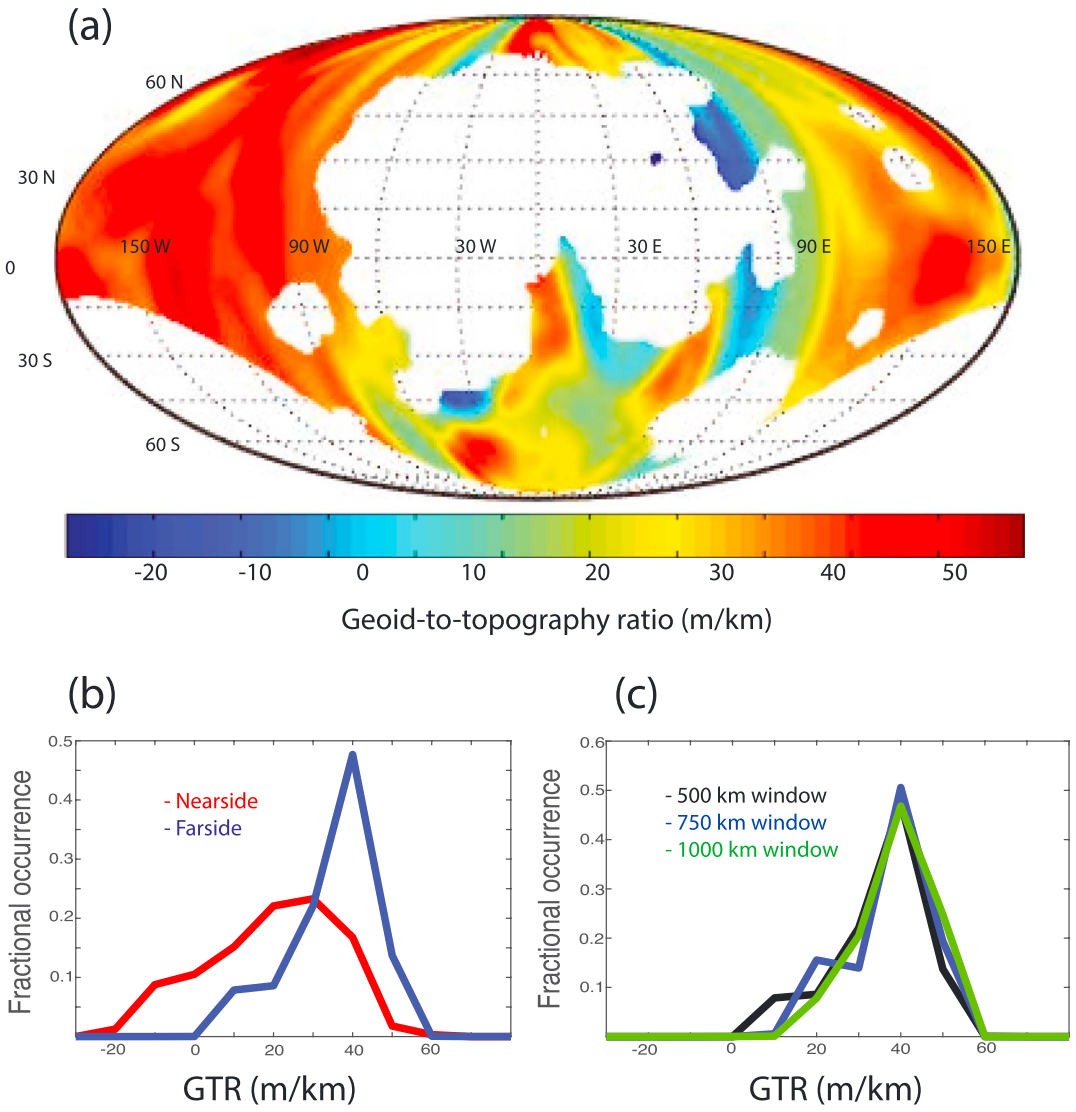


**Figure 3.** (a) Observed GTR values on the Moon calculated using a multitaper approach with localizing Slepian windows of radius 500 km. Areas where a circle of radius 500 km included more than 10% surface area of maria or the SPA basin interior are not shown and were excluded from subsequent analysis. The map is a Mollweide projection centered on the nearside. (b) Histograms of observed GTRs on the nearside and farside highlands using localizing Slepian windows of radius 500 km. (c) Histograms of observed GTRs for the farside highlands calculated using localizing Slepian windows of radius 500, 750, and 1,000 km.

The weighting function $W_l$ is the expected fractional power of the localized topography at degree $l$:

$$W_l = \frac{\langle S_{TT}(l) \rangle}{\sum_{i=l_{\min}}^{l_{\max}} \langle S_{TT}(i) \rangle}, \tag{6}$$

where the brackets denote the expected value. Since we are calculating the observed GTRs of the Moon using Slepian windows, this weighting function takes into account the properties of those localization windows and can be expressed in terms of the unlocalized topographic coefficients and Slepian window coefficients (see Appendix A). This technique represents a window-bias correction and ensures that the models have the same windowing bias as the observations, an essential property for our comparison. For

a single-layer Airy model compensated at the crust-mantle interface, the admittance $Z_l$ at degree $l$ is given by (Wieczorek & Phillips, 1997)

$$Z_l = \frac{4\pi\rho_c R^3}{M(2l+1)}\left[1-\left(\frac{R-T_c}{R}\right)^l\right], \tag{7}$$

where $R$ is the lunar radius, $M$ is the lunar mass, $T_c$ is the reference crustal thickness (i.e., the thickness at zero elevation), and $\rho_c$ is the density of the crust.

The above methodology is based on the premise that isostasy is achieved when crustal columns contain equal mass. We hereafter refer to this approach as the "equal masses" approach. However, recent workers have asserted that the equal masses approach does not accurately represent a state of equilibrium on a sphere (Beuthe et al., 2016; Hemingway & Matsuyama, 2017), even when the geometry of the sphere is considered when computing masses in crustal columns (Wieczorek & Phillips, 1997). Hemingway and Matsuyama (2017) argue that a more appropriate definition of isostasy is obtained when pressure differences are minimized along equipotential surfaces at depth (e.g., Turcotte et al., 1981). We hereafter refer to this approach as the "equal pressures" approach. Under the equal pressures approach, the admittance $Z_l$ at degree $l$ is given by

$$Z_l = \frac{4\pi\rho_c R^3}{M(2l+1)}\left[1-\frac{\left(\frac{R-T_c}{R}\right)^{l+4}}{1+\frac{4\pi\rho_c R^3}{3M}\left(\left(\frac{R-T_c}{R}\right)^3-1\right)}\right], \tag{8}$$

where all variables are the same as in equation (7).

One can also consider Airy models with two layers in the crust. A multilayered model changes the predicted admittances because it changes the mass distribution throughout the crust but remains consistent with the observed bulk density of the crust, effectively changing the depth of compensation. The admittance equations are those given by Wieczorek and Phillips (1997), as corrected by Pauer and Breuer (2008). For a two-layer Airy model in which an upper crust that varies in thickness overlies a lower crust of uniform thickness, the admittance at degree $l$ is

$$Z_l = \frac{4\pi\rho_c R^3}{M(2l+1)}\left[1-\left(\frac{R-T_{\mathrm{uc}}}{R}\right)^l\left[1+\frac{\rho_m-\rho_{\mathrm{lc}}}{\rho_{\mathrm{lc}}-\rho_{\mathrm{uc}}}\left(\frac{R-T_c}{R-T_{\mathrm{uc}}}\right)^2\right]^{-1}-\left(\frac{R-T_c}{R}\right)^l\left[1+\frac{\rho_{\mathrm{lc}}-\rho_{\mathrm{uc}}}{\rho_m-\rho_{\mathrm{lc}}}\left(\frac{R-T_{\mathrm{uc}}}{R-T_c}\right)^2\right]^{-1}\right], \tag{9}$$

where $T_c$ is the total crustal thickness at zero elevation, $T_{\mathrm{uc}}$ is the upper crustal thickness at zero elevation, and $\rho_{\mathrm{uc}}$, $\rho_{\mathrm{lc}}$, and $\rho_m$ are the densities of the upper crust, lower crust, and mantle, respectively. Finally, for a two-layer Airy model with a lower crust of variable thickness underlying a uniformly thick upper crust, the admittance at degree $l$ is

$$Z_l = \frac{4\pi\rho_c R^3}{M(2l+1)}\left[1+\left[\frac{\rho_{\mathrm{lc}}-\rho_{\mathrm{uc}}}{\rho_{\mathrm{uc}}}\left(\frac{R-T_{\mathrm{uc}}}{R}\right)^{l+2}\right]-\left(\frac{R-T_c}{R}\right)^l\left[1+\frac{\rho_{\mathrm{lc}}-\rho_{\mathrm{uc}}}{\rho_{\mathrm{uc}}}\left(\frac{R-T_{\mathrm{uc}}}{R}\right)^2\right]\right]. \tag{10}$$

These two models can be regarded as end-members. Equation (9) represents a two-layer crust for which the intercrustal boundary follows the crust-mantle interface; equation (10) represents a two-layer crust for which the intercrustal boundary follows the topography. Note that although equations (9) and (10) are for crustal layers, the variables may correspond to any layers of uniform density (i.e., including a layer in the uppermost mantle).

Equations (9) and (10) follow from the equal masses approach to isostasy. Two-layer models under the equal pressures approach (Hemingway & Matsuyama, 2017) have not previously been derived, so we derive such formulas here. For an Airy model with two layers in the crust, one in which the upper layer varies in thickness and overlies a uniformly thick lower layer, the admittance at degree $l$ is

$$Z_l = \frac{4\pi\rho_{\mathrm{uc}} R^3}{M(2l+1)}\left[1-\frac{\rho_{\mathrm{lc}}-\rho_{\mathrm{uc}}}{\rho_m-\rho_{\mathrm{uc}}}\left(\frac{R-T_{\mathrm{uc}}}{R}\right)^{l+2}-\frac{\rho_m-\rho_{\mathrm{lc}}}{\rho_m-\rho_{\mathrm{uc}}}\left(\frac{R-T_c}{R}\right)^{l+2}\right], \tag{11}$$

where the variables are the same as in equations (9) and (10). For a two-layer Airy model in which a lower crust that varies in thickness underlies an upper crust of uniform thickness, the admittance at degree *l* under the equal pressures approach is

$$Z_l = \frac{4\pi\rho_{uc}R^3}{M(2l+1)}\left[1+\frac{\rho_{lc}-\rho_{uc}}{\rho_{uc}}\left(\frac{R-T_{uc}}{R}\right)^{l+2}-\frac{\rho_{lc}}{\rho_{uc}}\left(\frac{R-T_c}{R}\right)^{l+2}\right], \tag{12}$$

where the variables are again the same as in equations (9) and (10). Equations (11) and (12) are derived in Appendix B. These two equations are derived under the assumption that the gravitational acceleration at the top and bottom of the crust is equal, an assumption that is approximately valid for the Moon but may not be for other planets (see section 4).

There is no analogous simple spherical admittance model for Pratt isostasy, so we used the approximation from equation (18) of Wieczorek and Phillips (1997), derived from expressions of Pratt-induced geoid anomalies on a sphere from Haxby and Turcotte (1978):

$$\mathrm{GTR} = \frac{\pi\rho_c R^2 T_c}{M}. \tag{13}$$

In equation (13), the density $\rho_c$ is the reference crustal density (i.e., density at zero elevation), and $T_c$ is the reference crustal thickness.

To guide the choice of parameters for our isostatic models, we considered the results of other studies. GRAIL observations (Wieczorek et al., 2013) combined with Apollo seismic data (e.g., Dainty et al., 1976; Nakamura et al., 1976; Goins et al., 1981; Nakamura, 1983; Khan & Mosegaard, 2002; Lognonné et al., 2003) show that the reference crustal thickness on the Moon is 34–43 km, and the average crustal density in the highlands is 2,550 kg/m$^3$. Measurement of the bulk density of lunar samples with the bead method and helium pycnometry (Kiefer et al., 2012) indicates that lunar mare basalts typically have bulk densities between 3,010 and 3,270 kg/m$^3$. Theoretical models of lunar magma ocean solidification and subsequent mantle overturn combined with calculation of mineral densities as a function of depth (Elkins-Tanton et al., 2011) predict an upper mantle density that monotonically increases with depth between ~3,000 and ~3,200 kg/m$^3$, with a discrete jump in density at ~700 km depth. Finally, whereas geophysical models often include a uniform density crust, a GRAIL-based study (Besserer et al., 2014) showed that most localized effective density spectra in the lunar highlands decrease with increasing spherical harmonic degree above degree and order ~100, a result consistent with a decrease of porosity (increase in bulk density) with depth in the upper ~10 km of the crust.

### 3.2. Results

GTR values for the Moon are shown in Figure 3a for the case with localizing Slepian windows constructed from spherical caps of radius 750 km. For a cap radius of 750 km, there are three Slepian windows with concentration factors $>$0.99. We define uncertainties as the standard error of GTR values over these three tapers. For most ($>$80%) locations on the Moon, these uncertainties are $<$3 m/km. We additionally test the mean GTRs for each individual taper. The three tapers yield a range in mean GTR for the nearside or farside highlands of $<$2 m/km. Therefore, variability among the tapers (i.e., different Slepian windows) does not have a large effect on our results.

Our focus is on the lunar highlands. On the nearside, many of the GTR values are negative at or near the lunar maria, reflecting the effect of high-density mare basalts preferentially located in areas of low nearside topography. We masked out regions where more than 10% of the area of our localizing window consists of lunar maria (Fortezzo & Hare, 2013) or SPA basin interior (Head et al., 2010). As with the test for Pratt isostasy, we considered the remaining regions as highlands. We found that the median nearside GTR value is $25.8^{+7.5}_{-5.7}$ m/km (where the bounds are the 25th and 75th percentile values), consistent with the 26.7 ± 6.9 m/km average value found by Wieczorek et al. (2006). In contrast, the median GTR value for the farside highlands is substantially higher at $39.3^{+5.7}_{-6.2}$ m/km (Figure 3b). A Kolmogorov-Smirnov test shows that the nearside and farside GTR distributions are statistically different at the 0.01% significance level. We report the median GTR rather than the mean GTR to account for possible asymmetry in GTR distribution (Figure 3b).

Our nominal case involved expansion of gravity and topography fields to degree and order 660, excluding degrees 1 and 2, but we performed tests with other expansions for robustness. Using localized fields

expanded only to degree and order 300 changed the resultant GTRs by an average of only ~0.1 m/km and a maximum of 1 m/km, whereas using fields expanded only to degree 100 changed the resultant GTRs by an average of ~5 m/km and a maximum of 15 m/km. The average differences in GTR are relatively small because the geoid emphasizes longer wavelengths. Though we filtered out degree 2 in these results as described above, we tested our calculations for cases in which degree 2 was included in the geoid and topography fields. We found that this inclusion caused the resultant distribution of GTRs to be broader than the case with degree 2 removed but did not change the mode of the distribution by more than 3 m/km. We also tested our calculations for cases in which both degree 1 and degree 2 were included, and we found that the mode of the distribution changed by less than 1 m/km compared with the case with only degree 1 filtered out. We also tested the sensitivity of our results to the choice of tapering bandwidth $L$. We found that analysis using localization with $L = 30$ changed the mean lunar GTR by only ~0.1 m/km compared with $L = 15$. Finally, we calculated GTRs spatially instead of spectrally. We found that performing linear regression between geoid and topography data sampled in a window of radius 500, 750, or 1,000 km changed the mean of the resulting GTRs by $<3$ m/km compared with cases using the same sized Slepian windows, but the distribution of GTRs was less broad than with the spectral approach. Note that even in this case of using a localizing window that is constant, the spectral properties of the window are taken into account when compared with modeled GTRs (see Appendix A).

Although GTR distribution is somewhat sensitive to the radius of the Slepian windows, our results hold for a range of window sizes (Figure 3c). We also tested for possible effects of some geologic structures. Large impact basins have a super-isostatic central region and a surrounding subisostatic annulus (Neumann et al., 1996, 2015; Andrews-Hanna, 2013; Melosh et al., 2013). Also, areas that appear to be highland terrain on the surface may contain cryptomaria, mare basalts covered by younger impact ejecta (Whitten & Head, 2015; Sori et al., 2016). When we excluded basins $>200$ km in diameter and proposed cryptomare regions from the analysis, the median GTR changed by $<1$ m/km. That this change was small is probably because cryptomare deposits are insufficiently massive to have large effects on isostatic state, and because the positive mass anomaly at the center of a basin is the result of isostatic adjustment of the entire basin during cooling and contraction of a large impact melt pool (Melosh et al., 2013) and is effectively counteracted in our analysis by the surrounding annular-shaped negative anomaly.

Predicted GTR values for single-layer Pratt and Airy models of the crust are shown in Figure 4. For the Airy models, we show results for models calculated using both the equal masses approach of equation (7) and the equal pressures approach of equation (8). For the inferred density and thickness of the lunar crust (Wieczorek et al., 2013), only those Airy models calculated with the equal pressures approach yield GTR values for the nearside and farside highlands equal to those observed. Similarly, examples of GTR values for two-layer crustal models of Airy isostasy, again taking into account localization of the data, are shown in Figure 5. These models, too, predict GTR values that are too low for appropriate model parameters with the equal masses approach to isostasy. This result holds particularly for the farside highlands, where the GTR values under the equal masses approach are inconsistent with either Airy or Pratt mechanisms for isostatic compensation entirely within the crust, unless we invoke improbably high values for average crustal thickness ($>60$ km), improbably high values of average crustal density ($>2{,}900$ kg/m$^3$), and/or a large density inversion with depth, for which there is no observational evidence. In contrast, under the equal pressures approach, observed GTR values are consistent with those predicted for a single-layer Airy model or with a two-layer Airy model.

In the equal pressures case, the GTRs correspond to an average crustal thickness of 47 km if topography is entirely compensated by Airy isostasy. This value is greater than the 34–43 km average crustal thickness values of Wieczorek et al. (2013), but we excluded the mare and SPA regions, where the crust is relatively thin. The average crustal thickness values of Wieczorek et al. (2013) in regions we studied are 39, 40, 48, and 49 km for the four different models they considered (these four models have, respectively, overall average crustal thickness values of 34, 35, 43, and 43 km and average crustal porosities of 12, 7, 12, and 7%). Converting the local crustal thickness to zero-elevation crustal thickness shows that it may be necessary to invoke some difference in the zero-elevation crustal thickness between the nearside and farside, providing caution against assuming that Airy isostasy is the only contributor to crustal thickness variations at the degree-1 scale.

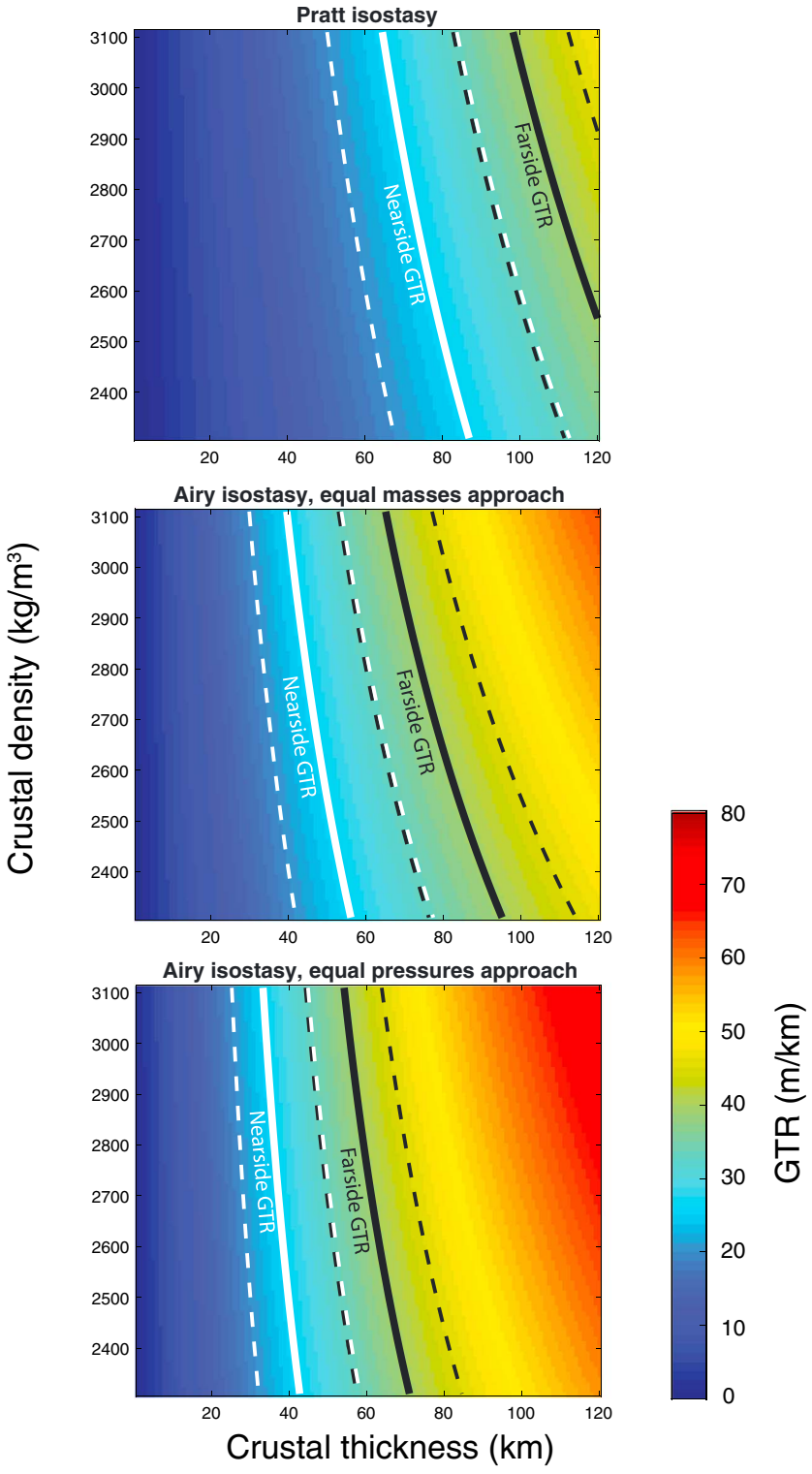


**Figure 4.** GTR values predicted for isostatic compensation of topography by variations in the density (top) or thickness of a single crustal layer according to the equal masses approach (middle) or equal pressures approach (bottom). For the top plot, the crustal density is the density at zero elevation; for the middle and bottom plots, the crustal thickness is the thickness at zero elevation. The median observed GTRs of the nearside highlands (25.8 m/km) are represented by solid white lines; the 25th (20.1 m/km) and 75th (33.1 m/km) percentile values are represented by dashed white lines. The median observed GTRs of the farside highlands (39.2 m/km) are represented by solid black lines; the 25th (33.1 m/km) and 75th (45.0 m/km) percentile values are represented by dashed black lines. For expected ranges in values of the Moon's average crustal thickness and density, the GTR values of these isostatic models match the observed GTRs of the highlands under Airy isostasy only with the equal pressures approach.

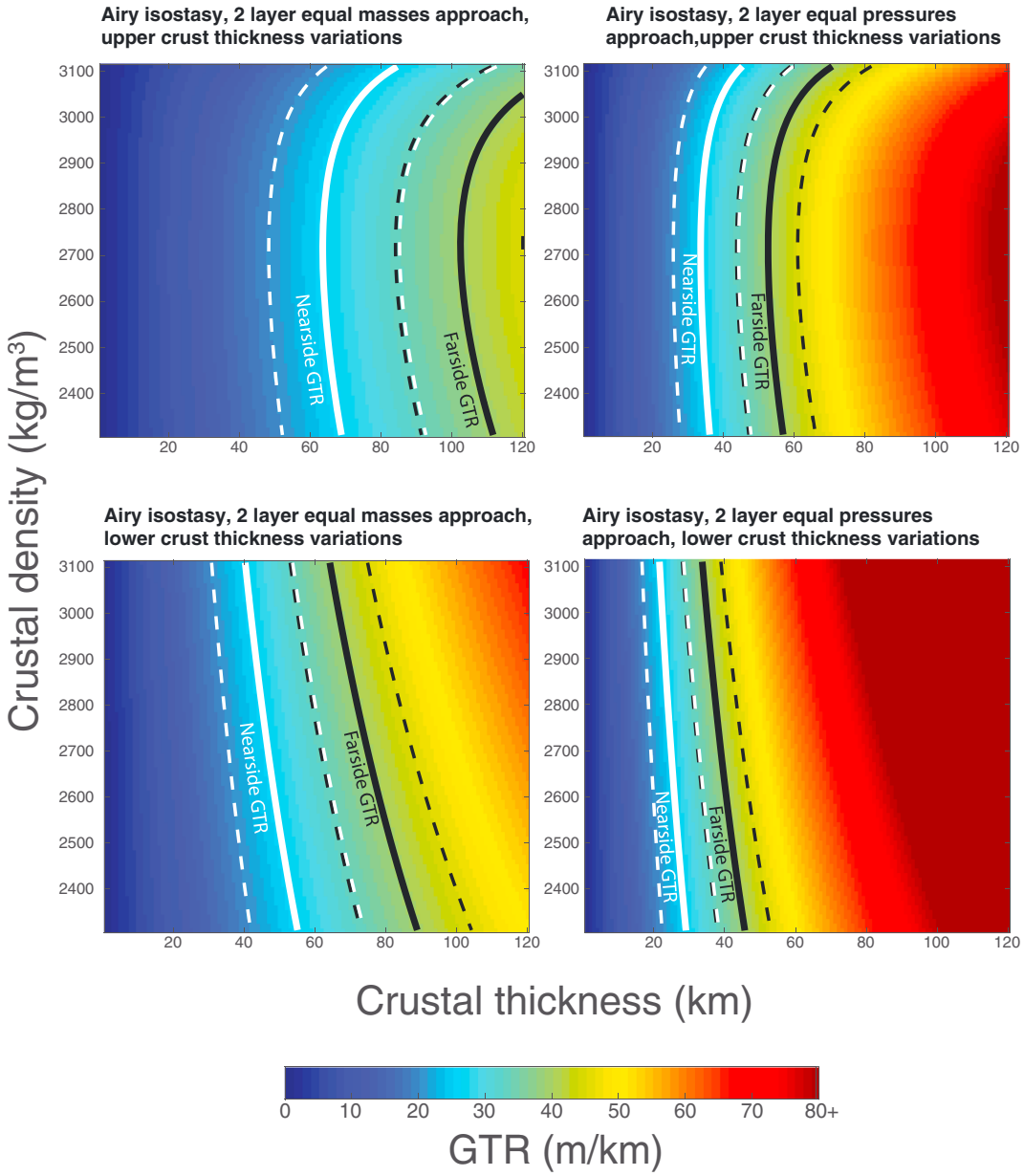


**Figure 5.** GTR values predicted for isostatic compensation of topography according to the equal masses approach (left column) or equal pressures approach (right column) by variations in the thickness of either an upper crustal layer (top row) or a lower crustal layer (bottom row), given a uniform thickness of the second crustal layer. The median observed GTRs of the nearside highlands (25.8 m/km) are represented by solid white lines; the 25th (20.1 m/km) and 75th (33.1 m/km) percentile values are represented by dashed white lines. The median observed GTRs of the farside highlands (39.2 m/km) are represented by solid black lines; the 25th (33.1 m/km) and 75th (45.0 m/km) percentile values are represented by dashed black lines. In all cases, the density of the lower crust is 300 kg/m$^3$ greater than that of the upper crust, the density of the underlying mantle is 3,400 kg/m$^3$, and the upper and lower crusts have equal average thickness values.

## 4. Discussion

The most direct interpretation of our results is that lunar topography is compensated under an Airy mechanism, and that the equal pressures approach to isostasy (Hemingway & Matsuyama, 2017) is the appropriate definition to represent a state of equilibrium. GTR values under the equal masses approach for compensation entirely with variations in thickness of the crust are too high, especially for the farside highlands. The farside GTR data may be fit under the equal masses approach if the upper mantle is involved in compensation. Under this interpretation, by adapting equation (9) for a layered model of a variably thick crust overlying a uniformly thick upper mantle, we found that an upper mantle >125 km thick and with a density of 3,000–3,220 kg/m$^3$

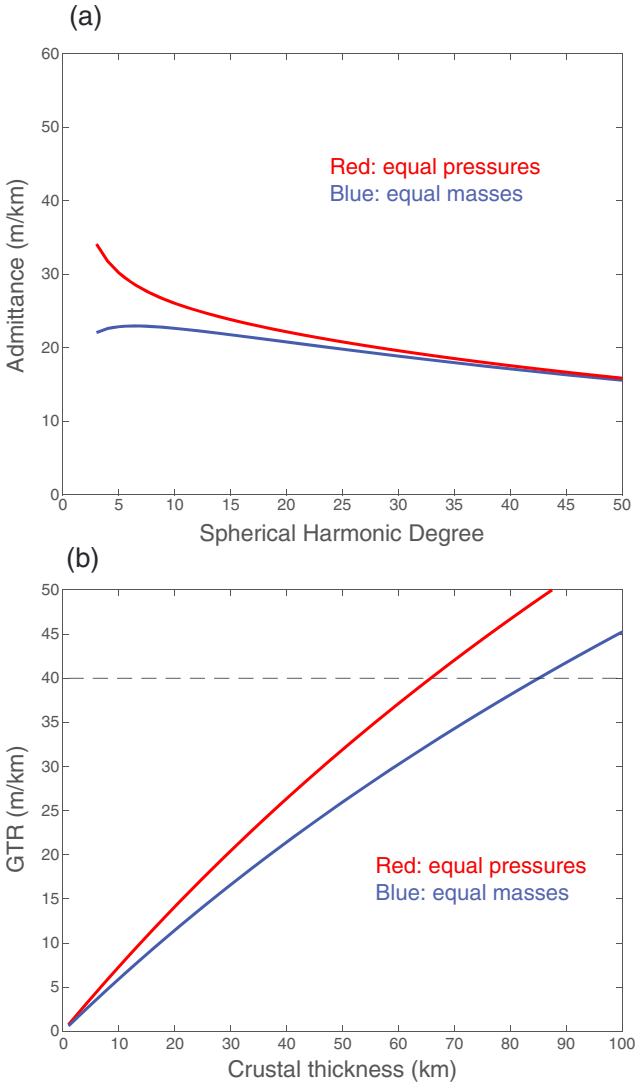


**Figure 6.** Quantification of the differences between the equal masses formulation (Wieczorek & Phillips, 1997) and the equal pressures formulation (Hemingway & Matsuyama, 2017) of single-layer Airy isostasy with a crustal density of 2,550 kg/m$^3$. (a) Degree-dependent admittances for both approaches. (b) Predicted GTR values for both approaches. The magnitude of the differences is highest for low spherical harmonic degrees and large crustal thicknesses (e.g., the farside). The horizontal dashed line corresponds to the median observed GTR for the farside highlands.

given a lower mantle density of 3,400 kg/m$^3$ can fit the observed farside GTRs. Such a relatively low mantle upper density could result from porosity (Wieczorek et al., 2013) or from different composition if the upper mantle is primarily Mg-rich orthopyroxene (enstatite) rather than Mg-rich olivine (forsterite) (Elkins-Tanton et al., 2011; Melosh et al., 2017).

The simpler explanation, and therefore the one that we favor here, is an interpretation of the GTR values under the equal pressures approach. With this approach, the observed GTR values of both the nearside and farside highlands can be reproduced with Airy models. It is worth noting that Hemingway and Matsuyama (2017) argued that the difference between the two approaches was relatively minor for the Moon, yielding results that differ by only ~27%. However, that statement was made in consideration only of the nearside GTRs of the Moon. For the lunar farside, where observed GTRs and crustal thickness are greater, the difference between the two approaches is more pronounced, as may be seen in Figure 6. This effect is consistent with our observations and models. The difference between the two approaches yields a relatively small difference in GTR on the nearside and a greater difference on the farside (i.e., the difference in the positions of the white lines in the middle and bottom panels of Figure 4 is smaller than those of the black lines). The dichotomy in observed GTR values between the nearside and farside (Figure 3b) thus may be a consequence of the hemispherical dichotomy in crustal thickness.

An alternative hypothesis to Airy compensation is flexural isostasy involving substantial lithospheric strength in areas of large topographic loads, an effect that would increase admittance values compared with a strict Airy model. The farside highlands, however, are thought to have formed very early in lunar history (Wasson & Warren, 1980; Jolliff et al., 2000), as a result of convective asymmetries in the magma ocean (Loper & Werner, 2002) or spatial variations in tidal heating (Garrick-Bethell et al., 2010, 2014). Additionally, flexural support predicts high admittances at low spherical harmonic degrees. The equation for the admittance at degree $l$ for a top-loaded flexural model (James et al., 2015) is given by

$$Z_l = \frac{4\pi\rho_c R^3}{M(2l+1)}\left[1-\left(\frac{R-T_c}{R}\right)^{l+2}\frac{1-\Gamma_1}{1-\Gamma_2+\frac{\rho_c}{\rho_m-\rho_c}e_l}\right], \quad (14)$$

where the variables are the same as in equations (7)–(12). A derivation of this equation, as well as the self-gravitational terms $\Gamma_1$ and $\Gamma_2$ and the parameter $e_l$, is given in Appendix C. This equation is derived under the assumption, also made in the derivation of equations (11) and (12), that the gravitational acceleration at the top and bottom of the crust is equal (see section 4).

We plot the expected admittances from this model in Figure 7a and the resulting expected GTRs in Figure 7b, and we compare both to the case of a single-layer Airy isostatic model under the equal pressures approach. For the observed crustal thickness on the Moon (Wieczorek et al., 2013), our observed GTR values are best fit with the Airy compensation model, as even a moderate elastic thickness causes predicted GTR values to be too high. For example, for an elastic thickness of 5 km, the best fit nearside GTR of 25.8 m/km corresponds to a crustal thickness of 7 km, whereas the upper bound nearside GTR of 33.3 m/km corresponds to a crustal thickness of 22 km. The effect of increasing elastic thickness is to increase admittances and therefore GTR. For an elastic thickness of 12 km or greater, even the upper bound on our observed farside GTR (45.0 m/km) is never reached for any crustal thickness. We therefore conclude that Airy isostasy is more likely to be the primary compensation mechanism.

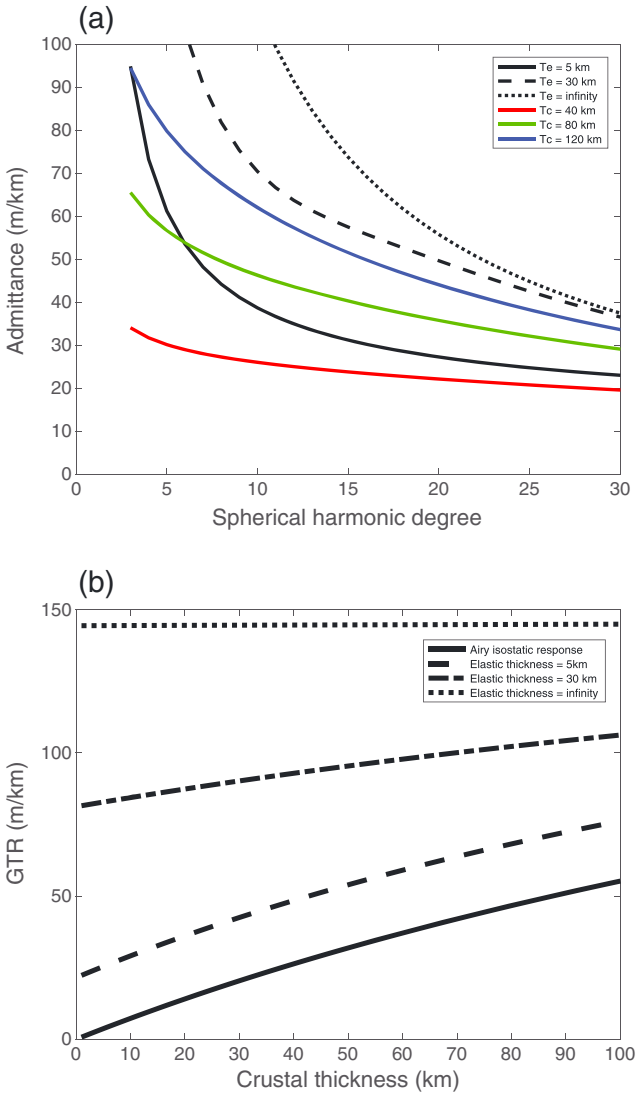


**Figure 7.** (a) Admittance values for several compensation models. Under flexure for a top-loaded lithosphere with a crustal thickness of 40 km and various elastic thicknesses (black lines), admittance is high at low degrees and low at high degrees. Under Airy isostasy for various crustal thicknesses (colored lines) under the equal pressures formulation, admittance varies less as a function of spherical harmonic degree. (b) GTRs as a function of crustal thickness for models of various elastic thickness and for the case of pure Airy isostasy. For the lunar crustal thickness of Wieczorek et al. (2013), the case of Airy isostasy fits observed GTRs better than cases with a flexural signal.

Dynamic compensation of topography, that is, support by mantle convection, can also result in similarly high GTR values compared with the equal masses Airy model, and such a process has been proposed for Earth (Ceuleneer et al., 1988) and Venus (Smrekar & Phillips, 1991). However, whereas convection may (Laneuville et al., 2013) or may not (Pritchard & Stevenson, 2000) have been important following magma ocean solidification and mantle overturn, the lunar mantle is unlikely to be convecting vigorously at present (Laneuville et al., 2013; Evans et al., 2014). Additionally, we do not observe an increase in mean GTR with increasing size of localizing window, which would be expected for dynamic compensation (James et al., 2013). Therefore, we conclude that gravity and topography data are most consistent with Airy isostasy, either in a single-layered crust or a two-layered crust.

Our results suggest that the formation of long-wavelength topography on the Moon preceded the development of a thick elastic lithosphere. This implication constrains the formation of the farside highlands in particular. If a substantial fraction of the thickness of the farside highlands consists of impact ejecta from the SPA basin-forming impact (Zuber et al., 1994) emplaced after the growth of an elastic lithosphere, the farside GTRs would be greater than presently observed (Figure 7b). Since Airy compensation in the crust is the more likely compensation mechanism, any contribution from top-loading flexure is relatively minor. Therefore, the farside highlands likely formed early in lunar history as a result of processes such as asymmetries in the magma ocean or spatial variability in tidal heating (Wasson & Warren, 1980; Jolliff et al., 2000; Loper & Werner, 2002; Garrick-Bethell et al., 2010, 2014; ). Alternatively, the farside highlands may include a substantial contribution from SPA ejecta if the basin-forming impact occurred sufficiently early in lunar history. This interpretation would require that there was no lithosphere with long-term strength immediately following basin formation, and that the timescale for relaxation of long-wavelength topography and crustal thickness variations by lateral crustal flow under Airy isostasy was longer than the development time of an elastic lithosphere thereafter.

A few caveats apply to our results. Equations (9)–(12) are based on the assumption that the gravitational acceleration at the surface is equal to the gravitational acceleration at the crust-mantle interface (and the lower crust-upper crust interface in the two-layer scenarios). The difference in acceleration at the two surfaces is minor for the Moon; for a crust with density 2,550 kg/m$^3$ and average thickness 40 km, we calculated the difference between gravitational acceleration at the surface and at the crust-mantle interface to be $<$1%. Finite-amplitude corrections are also neglected in equations (7)–(12) but are similarly minor in magnitude. Future work could consider a combination of top-loading and bottom-loading scenarios to reproduce observed admittances, as has been done for Mars (e.g., Lowry & Zhong, 2003). Our results here show that compensation occurring primarily with an Airy mechanism involving variations in crustal thickness is consistent with the high-resolution gravity and topography data. We interpret this scenario as correct because of its consistency with previous models of the formation of highland terrain, but it is possible that a complex combination of Airy isostasy, flexure from top loading, and flexure from bottom loading may also be mathematically consistent with observations. Flexural cases with either membrane stresses only or bending stresses only may also be considered as end-members, as it has been suggested that impacts may relieve one stress component (Freed et al., 2009).

## 5. Summary and Conclusions

A general lack of correlation between crustal density and topography shows that Pratt isostasy is not an important contributor to the isostatic compensation of the lunar highlands. Analysis of the Moon's GTRs reveals that the lunar highlands can be fit with a model of Airy compensation if isostasy is defined as a state in which equal pressures occur along equipotential surfaces at depth rather than a state in which crustal columns of a given surface area contain equal masses. An observed hemispherical dichotomy in GTR values, with farside highland GTRs ($39.3^{+5.7}_{-6.2}$ m/km) significantly greater than nearside highland GTRs ($25.8^{+7.5}_{-5.7}$ m/km), occurs as a result of a similar hemispherical difference in crustal thickness. The Airy isostatic model can be fit with either a single-layered crust or a two-layered crust. Flexural compensation is likely to be only a minor component of compensation at large scales because even a relatively small elastic thickness at the time of the formation of the topography yields GTRs higher than observed. Therefore, we conclude that GRAIL data reveal that long-wavelength topography of the Moon is primarily compensated by Airy isostasy. Our conclusion implies that this topography was formed early in lunar history before the development of a thick elastic lithosphere.

## Appendix A: Spectrally Derived GTRs

In this Appendix we derive equations (3) and (4), that it, the geoid-to-topography ratio (GTR) in the spectral domain. We start by assuming that the geoid $n$ and topography $t$ are expressed as a sum of spherical harmonic functions:

$$n(\theta,\phi)=\sum_{l=0}^{L}\sum_{m=-l}^{l}n_{lm}Y_{lm}(\theta,\phi) \tag{A1}$$

$$t(\theta,\phi)=\sum_{l=0}^{L}\sum_{m=-l}^{l}t_{lm}Y_{lm}(\theta,\phi), \tag{A2}$$

where $l$ and $m$ are spherical harmonic degree and order, respectively, $L$ is the maximum observed degree of geoid or topography, and $Y_{lm}$ are spherical harmonic functions. To determine the GTR in a particular region, we localize the data by multiplying the geoid and topography by the same localizing window $h(\theta, \Phi)$, also expressed in spherical harmonics:

$$h(\theta,\phi)=\sum_{l=0}^{L_h}\sum_{m=-l}^{l}h_{lm}Y_{lm}(\theta,\phi). \tag{A3}$$

Here $L_h$ is the maximum degree to which the localizing window is expanded. The localized geoid $N$ and topography $T$ are then simply given by multiplying equations (A1) and (A2) by equation (A3):

$$N(\theta,\phi)=h(\theta,\phi)n(\theta,\phi) \tag{A4}$$

$$T(\theta,\phi)=h(\theta,\phi)t(\theta,\phi). \tag{A5}$$

An example of a localizing window, localized geoid, and localized topography is shown in Figure 2. The GTR is the linear scaling factor, $a$, that best relates the localized topography to the localized geoid:

$$N(\theta,\phi)=aT(\theta,\phi)+b, \tag{A6}$$

where $b$ is the offset at zero topography. For some cases, this offset may be assumed to equal 0, but we derive the general case here. The values for $a$ and $b$ can be calculated by minimizing the misfit between the two localized fields in equation (A6) in a least squares sense by integrating over the area of the entire sphere $\Omega$. The term to be minimized is

$$\int_{\Omega}[N(\theta,\phi)-aT(\theta,\phi)-b]^2 d\Omega. \tag{A7}$$

We take the derivative of (A7) with respect to $a$ and $b$ and equate them to zero to obtain, respectively,

$$\int_{\Omega}-2\left(NT-aT^2-bT\right)d\Omega=0 \tag{A8}$$

$$\int_{\Omega}-2(N-aT-b)\ d\Omega=0. \tag{A9}$$

Parseval's theorem relates the integral of the product of two arbitrary functions, $f$ and $g$, on the sphere to their cross-power spectra:

$$\frac{1}{4\pi}\int_{\Omega}(f\times g)d\Omega=\sum_{l=0}^{\infty}S_{fg}. \tag{A10}$$

The cross-power spectrum of two arbitrary functions $f$ and $g$ is defined as

$$S_{fg}=\sum_{m=-l}^{l}f_{lm}g_{lm}. \tag{A11}$$

From equation (A10), equations (A8) and (A9) become

$$\sum_{l=0}^{L}S_{NT}=a\sum_{l=0}^{L}S_{TT}+bT_{00} \tag{A12}$$

$$N_{00}=aT_{00}+b. \tag{A13}$$

Solving this set of equations for the GTR $a$ yields

$$a=\frac{\sum_{l=0}^{L}S_{NT}-N_{00}T_{00}}{\sum_{l=0}^{L}S_{TT}-{T_{00}}^{2}}. \tag{A14}$$

If we wish to assume that the geoid is equal to 0 when the topography is equal to 0, we set $b$ = 0 in equations (A12) and (A13), and equation (A14) instead becomes

$$a=\frac{\sum_{l=0}^{L}S_{NT}}{\sum_{l=0}^{L}S_{TT}}. \tag{A15}$$

This GTR may then be compared with that predicted by equation (5):

$$\mathrm{GTR}=\sum_{l}W_lZ_l. \tag{A16}$$

Since we calculate observed GTRs using localization windows, this equation must take into account the spectral properties of those windows. The weighting function $W_l$ is the expected fractional power of the localized topography at degree $l$:

$$W_l=\frac{\langle S_{TT}(l)\rangle}{\sum_{i=l_{\min}}^{l_{\max}}\langle S_{TT}(i)\rangle}. \tag{A17}$$

The expected power of localized topography can be expressed in terms of the coefficients of unlocalized lunar topography and the coefficients of the localization window (Wieczorek, 2015):

$$\langle S_{TT}\rangle=\sum_{i=0}^{L}S_{hh}(j)\sum_{i-l1-il}^{l+j}S_{tt}(i)\left(C_{i0j0}^{l0}\right)^2, \tag{A18}$$

where $C$ is the Clesbsch-Gordan coefficient. For the case where the window is a simple constant, this weighting function reduces to

$$W_l=\frac{S_{tt(l)}}{\sum_{i=l_{\min}}^{l_{\max}}SS_{tt(i)}}. \tag{A19}$$

## Appendix B: Two-Layer Crustal Models of Airy Compensation

In this Appendix, we derive equations (11) and (12), the degree-dependent admittances for a two-layer crustal model compensated with thickness variations in the upper or lower crust under the equal pressures

approach of Hemingway and Matsuyama (2017). The geoid $n$ is given by summing the upward continued contributions from each interface (Wieczorek & Phillips, 1998):

$$Z_l = \frac{4\pi\rho_{\mathrm{uc}}R^3}{M(2l+1)}\left[\rho_{\mathrm{uc}}t(\theta,\varphi) - (\rho_{\mathrm{lc}}-\rho_{\mathrm{uc}})\left(\frac{R-T_{\mathrm{uc}}}{R}\right)^{l+2}w(\theta,\varphi) - (\rho_m-\rho_{\mathrm{lc}})\left(\frac{R-T_c}{R}\right)^{l+2}v(\theta,\varphi)\right], \tag{B1}$$

where $t$ is the topography, $w$ is the interface between the upper and lower crust, and $v$ is the relief on the interface between the lower crust and mantle. All other variables are the same as in previous equations. Under the equal pressures approach, the equation for isostatic equilibrium is

$$\rho_{\mathrm{uc}}gt = -(\rho_{lc}-\rho_{\mathrm{uc}})g_w w - (\rho_m-\rho_{\mathrm{lc}})g_v v, \tag{B2}$$

where $g$ is the gravitational acceleration at the surface, $g_{\mathrm{w}}$ is the gravitational acceleration at the interface between the upper and lower crust, and $g_{\mathrm{v}}$ is the gravitational acceleration at the interface between the lower crust and the mantle.

For the case of an upper crust that varies in thickness and a lower crust of uniform thickness, $w = v$. If we assume that the gravitational acceleration is approximately equal at each interface, equation (B2) reduces to

$$v = w = -\frac{\rho_{\mathrm{uc}}}{\rho_m-\rho_{\mathrm{uc}}}t \tag{B3}$$

By substituting equation (B3) into equation (B1), the admittance becomes

$$Z_l = \frac{4\pi\rho_{\mathrm{uc}}R^3}{M(2l+1)}\left[1 - \frac{\rho_{\mathrm{lc}}-\rho_{\mathrm{uc}}}{\rho_m-\rho_{\mathrm{uc}}}\left(\frac{R-T_{\mathrm{uc}}}{R}\right)^{l+2} - \frac{\rho_m-\rho_{\mathrm{lc}}}{\rho_m-\rho_{\mathrm{uc}}}\left(\frac{R-T_c}{R}\right)^{l+2}\right]. \tag{B4}$$

For the case of a lower crust that varies in thickness and an upper crust of uniform thickness, $w = t$. Under the assumption that the gravitational acceleration is approximately equal at each interface, equation (B2) reduces to

$$v = -\frac{\rho_{\mathrm{lc}}}{\rho_m-\rho_{\mathrm{lc}}}t \tag{B5}$$

By substituting equation (B5) into equation (B1), the admittance becomes

$$Z_l = \frac{4\pi\rho_{\mathrm{uc}}R^3}{M(2l+1)}\left[1 + \frac{\rho_{\mathrm{lc}}-\rho_{\mathrm{uc}}}{\rho_{\mathrm{uc}}}\left(\frac{R-T_{\mathrm{uc}}}{R}\right)^{l+2} - \frac{\rho_{\mathrm{lc}}}{\rho_{\mathrm{uc}}}\left(\frac{R-T_c}{R}\right)^{l+2}\right]. \tag{B6}$$

## Appendix C: Flexural Admittances Models for a Top-Loaded Lithosphere

The admittance function for a self-gravitating, top-loaded lithosphere was given by James et al. (2015), who used an equal mass definition for isostatic residual. In this Appendix, we derive a similar admittance using the equal pressure definition adopted in this paper. The relevant isostatic residual in this case is

$$(t-n) + \frac{\rho_m-\rho_c}{\rho_c}\frac{g_w}{g}\left(w-n'\right) + e_l F = 0. \tag{C1}$$

where $t$ is the topography, $n$ is the geoid, $w$ is the crust-mantle interface, $n'$ is the equipotential surface at the crust-mantle interface, $F$ is the flexural displacement of the lithosphere from an unstressed configuration, $e_l$ is a nondimensional flexural parameter, and all other variables are the same as in previous equations. In the top-loading scenarios considered here, the flexural displacement $F$ is equivalent to $w$. The nondimensional flexural parameter $e_l$ is given by the equation

$$e_l = \frac{D}{GMR^2\rho_c}\frac{-l^3(l+1)^3 + 4l^2(l+1)^2}{-l(l+1)+l-v} + \frac{ET_e}{GM\rho_c}\frac{-l(l+1)+2}{-l(l+1)+1-v} \tag{C2}$$

where $D$ is the flexural rigidity, $v$ is Poisson's ratio in the elastic shell, $T_e$ is the elastic thickness, and $E$ is the Young's modulus. For our calculations, we assumed a Poisson's ratio of $v = 0.25$ and a Young's modulus of $E = 10^{11}$ Pa. The flexural rigidity is itself a function of Poisson's ratio, Young's modulus, and elastic thickness and is given by the equation

$$D = \frac{ET_e{}^3}{12(1-v^2)}. \tag{C3}$$

The two terms in equation (C2) correspond to bending stresses and membrane stresses, respectively; one could calculate the flexural admittance considering only bending stresses or membrane stresses by setting the other term to zero.

The geoid $n$ at the planetary surface is a function of the two displaced interfaces, $t$ and $w$:

$$n_{lm} = \frac{4\pi\rho_c R^3}{M(2l+1)}\left[t_{lm} + \frac{\rho_m - \rho_c}{\rho_c}\left(\frac{R-T_c}{R}\right)^{l+2} w_{lm}\right] \tag{C4}$$

where the variables are the same as in equations (7)–(11). The comparable equipotential surface $n'$ at the crust-mantle boundary is

$$n'_{lm} = \frac{4\pi\rho_c R^3}{M(2l+1)}\left[\left(\frac{R-T_c}{R}\right)^{l} t_{lm} + \frac{\rho_m - \rho_c}{\rho_c}\frac{R-T_c}{R} w_{lm}\right]. \tag{C5}$$

Substituting (C5) into (C1) yields an isostatic residual that includes self-gravitation:

$$(1-\Gamma_1)t_{lm} + \frac{\rho_m - \rho_c}{\rho_c}\frac{g_w}{g}(1-\Gamma_2)w_{lm} + e_l w_{lm} = 0, \tag{C6}$$

where $\Gamma_1$ and $\Gamma_2$ are nondimensional terms that quantify self-gravitation. These terms are given by the equations

$$\Gamma_1 = \frac{4\pi\rho_c R^3}{M(2l+1)}\left[1 + \frac{\rho_m - \rho_c}{\rho_c}\frac{g_w}{g}\left(\frac{R-T_c}{R}\right)^{l}\right] \tag{C7}$$

and

$$\Gamma_2 = \frac{4\pi\rho_c R^3}{M(2l+1)}\left[\frac{g}{g_w}\left(\frac{R-T_c}{R}\right)^{l+2} + \frac{\rho_m - \rho_c}{\rho_c}\left(\frac{R-T_c}{R}\right)\right]. \tag{C8}$$

The ratio of crust-mantle interface relief to topography, $w/t$, then equals

$$\frac{w_{lm}}{t_{lm}} = -\frac{\rho_c}{\rho_m - \rho_c}\frac{g}{g_w}\left[\frac{(1-\Gamma_1)}{(1-\Gamma_2) + \frac{\rho_c g}{(\rho_m - \rho_c)g_w}e_l}\right]. \tag{C9}$$

Substituting (C9) into the equation for the geoid $N$ yields

$$n_{lm} = \frac{4\pi\rho_c R^3}{M(2l+1)}\left[1 - \frac{g}{g_w}\left(\frac{R-T_c}{R}\right)^{l+2}\frac{(1-\Gamma_1)}{(1-\Gamma_2) + \frac{\rho_c g}{(\rho_m - \rho_c)g_w}e_l}\right] t_{lm}. \tag{C10}$$

The geoid admittance $Z$ (as duplicated in equation (14)) is simply the ratio $n/t$. Under the assumption that the gravitational acceleration is approximately equal at each interface, $Z$ is

$$Z_l = \frac{4\pi\rho_c R^3}{M(2l+1)}\left[1 - \left(\frac{R-T_c}{R}\right)^{l+2}\frac{(1-\Gamma_1)}{(1-\Gamma_2) + \frac{\rho_c}{(\rho_m - \rho_c)}e_l}\right]. \tag{C11}$$

**Acknowledgments**
This study was supported by the GRAIL mission, which is part of NASA's Discovery Program and was performed under contract to the Massachusetts Institute of Technology and the Jet Propulsion Laboratory, California Institute of Technology. We thank Linda Elkins-Tanton for discussions on mineral densities at depth in the lunar mantle and Jeffrey Andrews-Hanna for discussions on the effects of the compensation states of large basins on our analysis. We thank Anthony Lowry and an anonymous reviewer for comments that greatly improved this manuscript. The GRAIL gravity and LOLA topography data sets used in this study are available from NASA's Planetary Data System archive. Derived data and model results from this paper are available at https://doi.org/10.6084/m9.figshare.5787924

## References

Andrews-Hanna, J. C. (2013). The origin of the non-mare mascon gravity anomalies in lunar basins. *Icarus*, *222*(1), 159–168. https://doi.org/10.1016/j.icarus.2012.10.031

Besserer, J., Nimmo, F., Wieczorek, M. A., Weber, R. C., Kiefer, W. S., McGovern, P. J., et al. (2014). GRAIL gravity constraints on the vertical and lateral density structure of the lunar crust. *Geophysical Research Letters*, *41*, 5771–5777. https://doi.org/10.1002/2014GL060240

Beuthe, M., Rivoldini, A., & Trinh, A. (2016). Enceladus's and Dione's floating ice shells supported by minimum stress isostasy. *Geophysical Research Letters*, *43*(19), 10,088–10,096. https://doi.org/10.1002/2016GL070650

Ceuleneer, G., Rabinowicz, M., Monnereau, M., Cazenave, A., & Rosemberg, C. (1988). Viscosity and thickness of the sub-lithospheric low-viscosity zone: Constraints from geoid and depth over oceanic swells. *Earth and Planetary Science Letters*, *89*(1), 84–102. https://doi.org/10.1016/0012-821X(88)90034-9

Dainty, A. M., Toksöz, M. N., & Stein, S. (1976). Seismic investigations of the lunar interior. *Proceedings of the Lunar Science Conference*, *7*, 3057–3075.

Elkins-Tanton, L. T., Burgess, S., & Yin, Q. (2011). The lunar magma ocean: Reconciling the solidification process with lunar petrology and geochronology. *Earth and Planetary Science Letters*, *304*(3-4), 326–336. https://doi.org/10.1016/j.epsl/2011/02.004

Evans, A. J., Zuber, M. T., Weiss, B. P., & Tikoo, S. M. (2014). A wet, heterogeneous lunar interior: Lower mantle and core dynamo evolution. *Journal of Geophysical Research: Planets*, *119*, 1061–1077. https://doi.org/10.1002/2013JE004494

Fortezzo, C. M., & Hare, T. M. (2013). Completed digital renovation of the 1:5,000,000 lunar geologic map series. Lunar Planet. Sci., 44, Abstract 2114.
Freed, A. M., Solomon, S. C., Watters, T. R., Phillips, R. J., & Zuber, M. T. (2009). Can Pantheon Fossae be the result of the Apollodorus crater-forming impact within the Caloris basin, Mercury? *Earth and Planetary Science Letters*, *285*(3-4), 320–327. https://doi.org/10.1016/j.epsl2009.02.038
Garrick-Bethell, I., Nimmo, F., & Wieczorek, M. A. (2010). Structure and formation of the lunar farside highlands. *Science*, *330*(6006), 949–951. https://doi.org/10.1126/science.1193424
Garrick-Bethell, I., Perera, V., Nimmo, F., & Zuber, M. T. (2014). The tidal-rotational shape of the Moon and evidence for polar wander. *Nature*, *512*(7513), 181–184. https://doi.org/10.1038/nature13639
Goins, N. R., Dainty, A. M., & Toksöz, M. N. (1981). Lunar seismology: The internal structure of the Moon. *Journal of Geophysical Research*, *86*(B6), 5061–5074. https://doi.org/10.1029/JB086iB06p05061
Harig, C., Lewis, K. W., Plattner, A., & Simons, F. J. (2015). A suite of software analyzes data on the sphere. *Eos, Transactions of the American Geophysical Union*, *96*. https://doi.org/10.1029/2015EO025851
Haxby, W. F., & Turcotte, D. L. (1978). On isostatic geoid anomalies. *Journal of Geophysical Research*, *83*(B11), 5473–5478. https://doi.org/10.1029/JB083iB11p05473
Head, J. W. (1975). Lunar mare deposits: Areas, volumes, sequence, and implication for melting in source areas. In *Conference on Origins of Mare Basalts and Their Implications for Lunar Evolution* (pp. 66–69). Houston: Lunar and Planetary Institute.
Head, J. W. (1982). Lava flooding of ancient planetary crusts: Geometry, thickness, and volumes of flooded lunar impact basins. *Earth, Moon, and Planets*, *26*(1), 61–88. https://doi.org/10.1007/BF00941369
Head, J. W., Fassett, C. I., Kadish, S. J., Smith, D. E., Zuber, M. T., Neumann, G. A., & Mazarico, E. (2010). Global distribution of large lunar craters: Implications for resurfacing and impactor populations. *Science*, *329*(5998), 1504–1507. https://doi.org/10.1126/science.1195050
Hemingway, D. J., & Matsuyama, I. (2017). Isostatic equilibrium in spherical coordinates and implications for crustal thickness on the Moon, Mars, Enceladus, and elsewhere. *Geophysical Research Letters*, *44*, 7695–7705. https://doi.org/10.1002/2017GL073334
Huang, Q., & Wieczorek, M. A. (2012). Density and porosity of the lunar crust from gravity and topography. *Journal of Geophysical Research*, *117*, E05003. https://doi.org/10.1029/2012JE004062
James, P. B., Zuber, M. T., & Phillips, R. J. (2013). Crustal thickness and support of topography on Venus. *Journal of Geophysical Research: Planets*, *118*, 859–875. https://doi.org/10.1029/2012JE004237
James, P. B., Zuber, M. T., Phillips, R. J., & Solomon, S. C. (2015). Support of long-wavelength topography on Mercury inferred from MESSENGER measurements of gravity and topography. *Journal of Geophysical Research: Planets*, *120*, 287–310. https://doi.org/10.1002/2014JE004713
Jolliff, B. L., Gillis, J. J., Haskin, L. A., Korotev, R. L., & Wieczorek, M. A. (2000). Major lunar crustal terranes: Surface expressions and crust-mantle origins. *Journal of Geophysical Research*, *105*(E2), 4197–4216. https://doi.org/10.1029/1999JE001103
Kaula, W. M., Schubert, G., Lingenfelter, R. E., Sjogren, W. L., & Wollenhaupt, W. R. (1974). Apollo laser altimetry and inferences as to lunar structure. *Proceedings of the Lunar Science Conference*, *5*, 3049–3058.
Keane, J. T., & Matsuyama, I. (2014). Evidence for lunar polar wander, and a past low-eccentricity, synchronous lunar orbit. *Geophysical Research Letters*, *41*, 6610–6619. https://doi.org/10.1002/2014GL061195
Khan, A., & Mosegaard, K. (2002). An enquiry into the lunar interior—A non-linear inversion of the Apollo lunar seismic data. *Journal of Geophysical Research*, *107*(E6), 5036. https://doi.org/10.1029/2001JE001658
Kiefer, W. S., Macke, R. J., Britt, D. T., Irving, A. J., & Consolmagno, G. J. (2012). The density and porosity of lunar rocks. *Geophysical Research Letters*, *39*, L03201. https://doi.org/10.1029/2012GL051319
Konopliv, A. S., Asmar, S. W., Carranza, E., Sjogren, W. L., & Yuan, D. N. (2001). Recent gravity models as a result of the Lunar Prospector mission. *Icarus*, *150*(1), 1–18. https://doi.org/10.1006/icar.2000.6573
Konopliv, A. S., Park, R. S., Yuan, D. N., Asmar, S. W., Watkins, M. M., Williams, J. G., et al. (2013). The JPL lunar gravity field to spherical harmonic degree 660 from the GRAIL primary mission. *Journal of Geophysical Research: Planets*, *118*, 1415–1434. https://doi.org/10.1002/jgre.20097
Konopliv, A. S., Park, R. S., Yuan, D. N., Asmar, S. W., Watkins, M. M., Williams, J. G., et al. (2014). High-resolution lunar gravity fields from the GRAIL primary and extended missions. *Geophysical Research Letters*, *41*, 1452–1458. https://doi.org/10.1002/2013GL059066
Kucinskas, A. B., Turcotte, D. L., & Arkani-Hamed, J. (1996). Isostatic compensation of Ishtar Terra, Venus. *Journal of Geophysical Research*, *101*(E2), 4725–4736. https://doi.org/10.1029/95JE02979
Lambeck, K., & Pullan, S. (1980). The lunar fossil bulge hypothesis revisited. *Physics of the Earth and Planetary Interiors*, *22*(1), 29–35. https://doi.org/10.1016/0031-9201(80)90097-7
Laneuville, M., Wieczorek, M. A., Breuer, D., & Tosi, N. (2013). Asymmetric thermal evolution of the Moon. *Journal of Geophysical Research: Planets*, *118*, 1435–1452. https://doi.org/10.1002/jgre.20103
Lemoine, F. G., Goossens, S., Sabaka, T. J., Nicholas, J. B., Mazarico, E., Rowlands, D. D., et al. (2013). High-degree gravity models from GRAIL primary mission data. *Journal of Geophysical Research: Planets*, *118*, 1676–1698. https://doi.org/10.1002/jgre.20118
Lemoine, F. G., Goossens, S., Sabaka, T. J., Nicholas, J. B., Mazarico, E., Rowlands, D. D., et al. (2014). GRGM900C: A degree-900 lunar gravity model from GRAIL primary and extended mission data. *Geophysical Research Letters*, *41*, 3382–3389. https://doi.org/10.1002/2014GL060027
Lemoine, F. G., Smith, D. E., Zuber, M. T., Neumann, G. A., & Rowlands, D. D. (1997). A 70th degree lunar gravity model (GLGM-2) from Clementine and other tracking data. *Journal of Geophysical Research*, *102*(E7), 16,339–16,359. https://doi.org/10.1029/97JE01418
Lognonné, P., Gagnepain-Beyneix, J., & Chenet, H. (2003). A new seismic model of the Moon: Implications for structure, thermal evolution and formation of the Moon. *Earth and Planetary Science Letters*, *211*(1-2), 27–44. https://doi.org/10.1016/S0012-821X(03)00172-9
Loper, D. E., & Werner, C. L. (2002). On lunar asymmetries, 1. Tilted convection and crustal asymmetry. *Journal of Geophysical Research*, *107*(E6), 5046. https://doi.org/10.1029/2000JE001441
Lowry, A. R., & Zhong, S. (2003). Surface versus internal loading of the Tharsis rise, Mars. *Journal of Geophysical Research*, *108*(E9), 5099. https://doi.org/10.1029/2003JE002111
Melosh, H. J., Freed, A. M., Johnson, B. C., Blair, D. M., Andrews-Hanna, J. C., Neumann, G. A., et al. (2013). The origin of lunar mascon basins. *Science*, *340*(6140), 1552–1555. https://doi.org/10.1126/science.1235768
Melosh, H. J., Kendall, J., Horgan, B., Johnson, B. C., Bowling, T., Lucey, P. G., & Taylor, G. J. (2017). South Pole-Aitken basin ejecta reveal the Moon's upper mantle. *Geology*, *45*(12), 1063–1066. https://doi.org/10.1130/G39375.1
Muller, P. M., & Sjogren, W. L. (1968). Mascons: Lunar mass concentrations. *Science*, *161*(3842), 680–684. https://doi.org/10.1126/science.161.3842.680
Nakamura, Y. (1983). Seismic velocity structure of the lunar mantle. *Journal of Geophysical Research*, *88*(B1), 677–686. https://doi.org/10.1029/JB088iB01p00677

Nakamura, Y., Duennebier, F. K., Latham, G. V., & Dorman, H. J. (1976). Structure of the lunar mantle. *Journal of Geophysical Research*, *81*(26), 4818–4824. https://doi.org/10.1029/JB081i026p04818

Neumann, G. A., Zuber, M. T., Smith, D. E., & Lemoine, F. G. (1996). The lunar crust: Global structure and significance of major basins. *Journal of Geophysical Research*, *101*(E7), 16,841–16,863. https://doi.org/10.1029/96JE01246

Neumann, G. A., Zuber, M. T., Wieczorek, M. A., Head, J. W., Baker, D. M. H., Solomon, S. C., et al. (2015). Lunar impact basins revealed by Gravity Recovery and Interior Laboratory measurements. *Science Advances*, *1*(9), e1500852. https://doi.org/10.1126/sciadv.1500852

O'Keefe, J. A. (1978). Isostasy on the Moon. *Science*, *162*(3860), 1405–1406. https://doi.org/10.1126/science.162.3860.1405

Padovan, S., Wieczorek, M. A., Margot, J. L., Tosi, N., & Solomon, S. C. (2015). Thickness of the crust of Mercury from geoid-to-topography ratios. *Geophysical Research Letters*, *42*, 1029–1038. https://doi.org/10.1002/2014GL062487

Pauer, M., & Breuer, D. (2008). Constraints on the maximum crustal density from gravity-topography modeling: Applications to the southern highlands of Mars. *Earth and Planetary Science Letters*, *276*(3-4), 253–261. https://doi.org/10.1016/j/epsl/2008.09.014

Prettyman, T. H., Hagerty, J. J., Elphic, R. C., Feldman, W. C., Lawrence, D. J., McKinney, G. W., & Vaniman, D. T. (2006). Elemental composition of the lunar surface: Analysis of gamma ray spectroscopy data from Lunar Prospector. *Journal of Geophysical Research*, *111*, E12007. https://doi.org/10.1029/2005JE002656

Pritchard, M. E., & Stevenson, D. J. (2000). Thermal aspects of lunar origin by giant impact. In R. M. Canup & K. Righter (Eds.), *Origin of the Earth and Moon*, (pp. 179–196). Tucson: University of Arizona Press.

Simons, F. J., Dahlen, F. A., & Wieczorek, M. A. (2006). Spatiospectral concentration on a sphere. *SIAM Review*, *48*(3), 504–536. https://doi.org/10.1137/S0036144504445765

Slepian, D., & Pollak, H. O. (1961). Prolate spheroidal wave functions, Fourier analysis and uncertainty I. *Bell System Technical Journal*, *40*(1), 43–63. https://doi.org/10.1002/j.1538-7305.1961.tb03976.x

Smith, D. E., Zuber, M. T., Neumann, G. A., & Lemoine, F. G. (1997). Topography of the Moon from the Clementine lidar. *Journal of Geophysical Research*, *102*(E1), 1591–1611. https://doi.org/10.1029/96JE02940

Smith, D. E., Zuber, M. T., Neumann, G. A., Mazarico, E., Lemoine, F. G., Head, J. W., et al. (2016). Summary of the results from the Lunar Orbiter Laser Altimeter after seven years in lunar orbit. *Icarus*, *283*, 70–91. https://doi.org/10.1016/j.icarus.2016.06.066

Smrekar, S. E., & Phillips, R. J. (1991). Venusian highlands: Geoid to topography ratios and their implications. *Earth and Planetary Science Letters*, *107*(3-4), 582–597. https://doi.org/10.1016/0012-821X(91)90103-O

Soderblom, J. M., Evans, A. J., Johnson, B. C., Melosh, H. J., Miljković, K., Phillips, R. J., et al. (2015). The fractured Moon: Production and saturation of porosity in the lunar highlands from impact cratering. *Geophysical Research Letters*, *42*, 6939–6944. https://doi.org/10.1002/2015GL065022

Solomon, S. C. (1978). The nature of isostasy on the Moon: How big a Pratt-fall for Airy models? *Proceedings of the Lunar and Planetary Science Conference*, *9*, 3499–3511.

Sori, M. M., Zuber, M. T., Head, J. W., & Kiefer, W. S. (2016). Gravitational search for cryptovolcanism on the Moon: Evidence for large volumes of early igneous activity. *Icarus*, *273*, 284–295. https://doi.org/10.1016/j.icarus.2016.02.009

Turcotte, D. L., Willemann, R. J., Haxby, W. F., & Norberry, J. (1981). Role of membrane stresses in the support of planetary topography. *Journal of Geophysical Research*, *86*(B5), 3951–3959. https://doi.org/10.1029/JB086iB05p03951

Wasson, J. T., & Warren, P. H. (1980). Contribution of the mantle to the lunar asymmetry. *Icarus*, *44*(3), 752–771. https://doi.org/10.1016/0019-1035(80)90142-6

Wetherill, G. W. (1975). Possible slow accretion of the Moon and its thermal and petrological consequences. In *Conference on Origins of Mare Basalts and Their Implications for Lunar Evolution* (pp. 184–188). Houston: Lunar and Planetary Institute.

Whitten, J. L., & Head, J. W. (2015). Lunar cryptomaria: Physical characteristics, distribution, and implications for ancient volcanism. *Icarus*, *247*, 150–171. https://doi.org/10.1016/j.icarus.2014.09.031

Wieczorek, M. A. (2015). Gravity and topography of the terrestrial planets. In G. Schubert (Ed.), *Physics of Terrestrial Planets and Moons*, *Treatise on Geophysics* (Vol. 10, pp. 153–193). Amsterdam: Elsevier.

Wieczorek, M. A., Jolliff, B. L., Khan, A., Pritchard, M., Weiss, B. P., Williams, J. G., et al. (2006). The constitution and structure of the lunar interior. *Reviews in Mineralogy and Geochemistry*, *60*(1), 221–364. https://doi.org/10.2138/rmg.2006.60.3

Wieczorek, M. A., Neumann, G. A., Nimmo, F., Kiefer, W. S., Taylor, G. J., Melosh, H. J., et al. (2013). The crust of the Moon as seen by GRAIL. *Science*, *339*(6120), 671–675. https://doi.org/10.1126/science.1231530

Wieczorek, M. A., & Phillips, R. J. (1997). The structure and compensation of the lunar highland crust. *Journal of Geophysical Research*, *102*(E5), 10,933–10,943. https://doi.org/10.1029/97JE00666

Wieczorek, M. A., & Phillips, R. J. (1998). Potential anomalies on a sphere: Applications to the thickness of the lunar crust. *Journal of Geophysical Research*, *103*(E1), 1715–1724. https://doi.org/10.1029/97JE03136

Wieczorek, M. A., & Simons, F. J. (2007). Minimum-variance multitaper spectral estimation on the sphere. *Journal of Fourier Analysis and Applications*, *13*(6), 665–692. https://doi.org/10.1007/s00041-006-6904-1

Zuber, M. T., Smith, D. E., Lehman, D. H., Hoffman, T. L., Asmar, S. W., & Watkins, M. M. (2013). Gravity Recovery and Interior Laboratory (GRAIL): Mapping the lunar interior from crust to core. *Space Science Reviews*, *178*(1), 3–24. https://doi.org/10.1007/s11214-012-9952-7

Zuber, M. T., Smith, D. E., Lemoine, F. G., & Neumann, G. A. (1994). The shape and internal structure of the Moon from the Clementine mission. *Science*, *266*(5192), 1839–1843. https://doi.org/10.1126/science.266.5192.1839

Zuber, M. T., Smith, D. E., Watkins, M. M., Asmar, S. W., Konopliv, A. S., Lemoine, F. G., et al. (2013). Gravity field of the Moon from the Gravity Recovery and Interior Laboratory (GRAIL) mission. *Science*, *339*(6120), 668–671. https://doi.org/10.1126/science.1231507